

MERGER-INDUCED SHOCKS IN THE NEARBY LIRG VV 114 THROUGH METHANOL OBSERVATIONS
WITH ALMATOSHIKI SAITO^{1,2}, DAISUKE IONO^{2,3}, DANIEL ESPADA^{2,3}, KOUICHIRO NAKANISHI^{2,3}, JUNKO UEDA⁴, HAJIME SUGAI⁵, SHURO TAKANO⁶, MIN S. YUN⁷, MASATOSHI IMANISHI⁸, SATOSHI OHASHI^{1,2}, MINJU LEE^{1,2}, YOSHIAKI HAGIWARA⁹, KENTARO MOTOHARA¹⁰, AND RYOHEI KAWABE^{1,2,3}(Received August 30, 2016; Revised October 10, 2016; Accepted November, 4, 2016)
Draft version June 23, 2021

ABSTRACT

We report the detection of two CH₃OH lines ($J_K = 2_K-1_K$ and 3_K-2_K) between the progenitor's disks (“Overlap”) of the mid-stage merging galaxy VV 114 obtained using the Atacama Large Millimeter/submillimeter Array (ALMA) Band 3 and Band 4. The detected CH₃OH emission show an extended filamentary structure (~ 3 kpc) across the progenitor's disks with relatively large velocity width (FWZI ~ 150 km s⁻¹). The emission is only significant in the “overlap” and not detected in the two merging nuclei. Assuming optically-thin emission and local thermodynamic equilibrium (LTE), we found the CH₃OH column density relative to H₂ ($X_{\text{CH}_3\text{OH}}$) peaks at the “Overlap” ($\sim 8 \times 10^{-9}$), which is almost an order of magnitude larger than that at the eastern nucleus. We suggest that kpc-scale shocks driven by galaxy-galaxy collision may play an important role to enhance the CH₃OH abundance at the “Overlap”. This scenario is consistent with that shock-induced large velocity dispersion components of ionized gas have been detected in optical wavelength at the same region. Conversely, low $X_{\text{CH}_3\text{OH}}$ at the nuclear regions might be attributed to the strong photodissociation by nuclear starbursts and/or putative active galactic nucleus (AGN), or inefficient production of CH₃OH on dust grains due to initial high temperature conditions (i.e., desorption of the precursor molecule, CO, into gas-phase before forming CH₃OH on dust grains). These ALMA observations demonstrate that CH₃OH is a unique tool to address kpc-scale shock-induced gas dynamics and star formation in merging galaxies.

Subject headings: galaxies: individual (VV 114, IC 1623, Arp 236) — galaxies: interactions — radio lines: galaxies

1. INTRODUCTION

Bright thermal rotational transitions of methanol (CH₃OH) are often used as a tracer of extragalactic shocks, which is established by a large number of unbiased wide-band mm/sub-mm molecular line surveys toward galaxies over the last decade (Takano et al. 2014, and references therein). Extragalactic CH₃OH observations found that some of the galaxies have $X_{\text{CH}_3\text{OH}}$ larger than $\sim 10^{-8}$ at the nuclei, arms, and bars with ~ 100 pc resolution (e.g., IC 342; Meier & Turner 2005). Purely gas-phase chemistry cannot explain these observational evidences, because the formation process of CH₃OH in gas-phase is not efficient to produce $X_{\text{CH}_3\text{OH}}$ greater than $\sim (1-3) \times 10^{-9}$ (Lee et al. 1996). Alternatively, high CH₃OH abundance is believed to arise from a series of hydrogenations of CO on dust grain surfaces under a low-temperature (~ 10 K) condition (Watanabe et al. 2003), because interstellar icy mantles are rich in CH₃OH ($\sim 10^{-6}$; e.g., Schutte et al. 1991). After the production on dust, it requires high temperature (i.e., hot-core chemistry; e.g., Garrod et al. 2008) or energetic heating (i.e., shock chemistry; e.g., Viti et al. 2011) mechanisms to heat the dust and then sublime CH₃OH into gas-phase. On the other hand, CH₃OH molecules are easily destroyed by UV radiation due to starburst or AGN without shielding ($A_V \sim 5$; Martín et al. 2009). Thus,

CH₃OH requires hot-core like or shocked ISM without strong UV radiation field to achieve an observable abundance. When hot-core like environment is excluded, CH₃OH lines become an excellent extragalactic shock tracer in molecular ISM.

However, most of the previous studies had mainly focused on nearby, bright galaxies or their nuclear regions so far (Henkel et al. 1987; Meier & Turner 2005; Martín et al. 2006a,b; Usero et al. 2006; García-Burillo et al. 2010; Aladro et al. 2011; Costagliola et al. 2011; Martín et al. 2011; Meier & Turner 2012; Davis et al. 2013; Meier et al. 2014; Takano et al. 2014; Watanabe et al. 2014; Aladro et al. 2015; Costagliola et al. 2015; Nakajima et al. 2015; Galametz et al. 2016; Nishimura et al. 2016). In this paper, we present multiple CH₃OH line observations toward the nearby merging galaxy VV 114, which are follow-up observations of our previous CH₃OH (2_K-1_K) detection at Overlap (Saito et al. 2015), in order to test kpc-scale shocks in molecular ISM due to a gas-rich galaxy-galaxy collision.

VV 114 is one of the local luminous infrared galaxies ($D_L = 87$ Mpc, $L_{\text{IR}} = 10^{11.69} L_\odot$; Armus et al. 2009). It is considered to be a mid-stage gas-rich major merger with the nuclear separation of ~ 6 kpc. The system has a (molecular and ionized) gaseous and dust filamentary structure (~ 4 kpc) across the galaxy disks (Yun et al. 1994; Frayer et al. 1999; Iono et al. 2004; Wilson et al. 2008; Rich et al. 2011; Iono et al. 2013; Sliwa et al. 2013; Saito et al. 2015; Tateuchi et al. 2015), which is not found in optical, FUV, and X-ray images (Scoville et al. 2000;

toshiki.saito@nao.ac.jp

¹ Department of Astronomy, The University of Tokyo, 7-3-1 Hongo, Bunkyo-ku, Tokyo 113-0033, Japan

Goldader et al. 2002; Grimes et al. 2006).

Our previous ALMA observations (Iono et al. 2013; Saito et al. 2015) revealed that the filament has multiple star-forming dense gas clumps at Overlap, one of which only has a CH_3OH (2_K-1_K) peak. In contrast, two massive clumps in the eastern nucleus, which harbor compact starburst (“SB”) and putative hard X-ray AGN (“AGN”), are bright in CN, HCN, and HCO^+ lines. This indicates that VV 114 has kpc-scale chemical variations along the filament. However, since we were only able to observe ten molecular lines, the chemical composition in the filament is not fully understood, and thus we followed up VV 114 with ALMA spectral scan mode.

We assumed $H_0 = 70 \text{ km s}^{-1} \text{ Mpc}^{-1}$, $\Omega_M = 0.3$, $\Omega_\Lambda = 0.7$ ($1'' = 420 \text{ pc}$) throughout this paper.

2. OBSERVATIONS AND DATA OVERVIEW

We observed VV 114 using Band 3 and Band 4 of ALMA with the spectral scan mode (Mathys et al. 2013) as a cycle 2 program (ID: 2013.1.01057.S). The correlator was configured to cover 84 - 111 GHz and 127 - 154 GHz using eight tunings. In this paper, we present the tunings containing the multiple CH_3OH (2_K-1_K) ($\nu_{\text{obs}} \sim 94.84 \text{ GHz}$) and CH_3OH (3_K-2_K) ($\nu_{\text{obs}} \sim 142.24 \text{ GHz}$) lines. We observed blended sets of thermal rotational transitions of CH_3OH . Detected transitions are listed in Table 1. Other transitions (e.g., $J_K = 0_0-1_{-1}$) are not robustly detected. Since such non-detections do not put meaningful upper limits in the analysis shown later, we ignore them in this paper. We will discuss some non-detected molecular lines in Saito et al. in preparation. The CH_3OH (2_K-1_K) data (Band 3) were obtained on 2014 July 3, 2014 July 4, and 2015 June 11 with the double-sideband system temperature (T_{sys}) of 39 - 103 K, whereas the CH_3OH (3_K-2_K) data (Band 4) was obtained on 2015 May 25 with T_{sys} of 47 - 124 K. Thirty-one to thirty-eight (thirty-six) 12 m antennas with the projected baseline length of 19 - 778 m (21 - 539 m) were assigned for the Band 3 (Band 4) observations. Each tuning has four spectral windows to cover each sideband. The spectral window has a bandwidth of 1.875 GHz with 1.938 MHz resolution, while they were binned together to create better signal-to-noise (S/N) data cubes. The total on-source time of the Band 3 and Band 4 observations are 47.4 min. and 20.0 min., respectively. Neptune and Uranus were used for the flux calibration of the both bands. J0137-2430 and J2258-2758 were used for the bandpass calibration of the both bands. Either of one of J0116-2052 and J0110-0741 was used for the phase calibration of Band 3, whereas J0110-0741 was used for that of Band 4.

The data reduction, calibration, and imaging were carried out using CASA (McMullin et al. 2007). All maps are reconstructed with the natural weighting to minimize noise rms levels. We made the data cubes with a velocity resolution of 50 km s^{-1} ($\sim 14.4 \text{ MHz}$) for CH_3OH (2_K-1_K) and 20 km s^{-1} ($\sim 9.8 \text{ MHz}$) for CH_3OH (3_K-2_K). Before imaging, we combined the cycle 0 CH_3OH (2_K-1_K) data (ID: 2011.0.00467.S) in order to increase the sensitivity, and continuum emission was subtracted in the uv -plane. We note that we re-calibrated the cycle 0 data using Butler-JPL-Horizons 2012 model. Other imaging properties are listed in Table 1, and will be introduced in detail by Saito et al. in preparation. The

systematic error of absolute flux scaling factor using a solar system object is 5% for Band 3 and Band 4 (Lundgren et al. 2013). The flux densities of the bandpass and phase calibrators were in good agreement with measurements provided by the ALMA Calibrator Source Catalogue². We ignore the difference of missing flux effect between Band 3 and Band 4, since the maximum recoverable scale of the assigned configuration for the Band 3 and Band 4 observations ($18''$ and $13''$, respectively) is comparable or larger than the filament of VV 114 detected in ^{13}CO (1-0) and dust continuum (Saito et al. 2015).

3. RESULTS

Images of the integrated intensity, velocity field, and velocity dispersion are shown in Figure 1. The total CH_3OH (2_K-1_K) and CH_3OH (3_K-2_K) integrated intensities are 0.91 ± 0.11 and $2.31 \pm 0.18 \text{ Jy km s}^{-1}$, respectively. We checked possible blending with other species using the molecular line database Splatalogue³ and also line detections reported by Watanabe et al. (2014), Aladro et al. (2015) and Costagliola et al. (2015), because some extragalactic line surveys reached line confusion limits. We found no potential bright lines around CH_3OH (2_K-1_K). Although there is $c\text{-C}_3\text{H}_2$ ($3_{12}-2_{21}$) ($\nu_{\text{rest}} = 145.08961 \text{ GHz}$) around CH_3OH (3_K-2_K) ($\nu_{\text{rest}} = 145.09-145.14 \text{ GHz}$), its contribution to the CH_3OH (3_K-2_K) intensities may be negligible because any other $c\text{-C}_3\text{H}_2$ transitions are not robustly detected toward the Overlap region in our Band 3/4 data. This is consistent with that the starburst galaxy NGC 253, which is thought to be dominated by shocks, shows weaker $c\text{-C}_3\text{H}_2$ line emissions than the CH_3OH (2_K-1_K) line (Aladro et al. 2015). Toward SB (Figure 2), we detected some $c\text{-C}_3\text{H}_2$ transitions (e.g., $J_{KaKc} = 4_{04}-3_{13}$), which is not stronger than CH_3OH (3_K-2_K), so CH_3OH (3_K-2_K) intensity might be slightly overestimated. However, this does not change our discussion and conclusion (see Section 4).

Figure 1 shows an extended filamentary structure which coincides with previous molecular gas and dust images (Iono et al. 2013; Saito et al. 2015). The strongest peak is located at Overlap, whereas the emission is only marginally detected in the stellar nuclei seen in Ks-band (Figure 2c). The global distribution is consistent with ^{13}CO and HCO^+ lines (molecular gas; Iono et al. 2013; Saito et al. 2015) and $880 \mu\text{m}$ continuum (dust; Figure 2a), although all of them except for CH_3OH show strong peaks at AGN and SB. In contrast, CH_3OH does not coincide with Paschen α emission (H_{II} regions and/or ionized gas shocks; Figure 2b). Ks-band continuum, mainly tracing old stellar component (Figure 2c), has no peaks at Overlap. This indicates that the CH_3OH filament of VV 114 is a relatively young structure compared with the age of the progenitor galaxies, which is likely due to a galaxy-galaxy collision as predicted by numerical simulations of a gas-rich major merger (Saitoh et al. 2009; Teyssier et al. 2010). These morphological comparisons suggest that CH_3OH lines trace a kpc-scale gas structure at the collision interface of the galaxy-galaxy interaction. To determine physical properties of Overlap,

² <https://almascience.nrao.edu/sc/>

³ <http://www.splatalogue.net/>

we employ the rotation diagram method (Goldsmith & Langer 1999) in the next Section.

4. LTE CALCULATION OF ROTATION TEMPERATURE AND COLUMN DENSITY

Assuming LTE and optically thin conditions for the CH₃OH lines, we can estimate the column density ($N_{\text{CH}_3\text{OH}}$) and rotation temperature (T_{rot}) using the rotation diagram. However, we need a special treatment in the case of VV 114, because the detected CH₃OH emission were blended by multiple *A*-type and *E*-type rotational transitions (e.g., Rabli & Flower 2010) due to the coarse velocity resolution and observed large velocity widths ($\text{FWZI} \sim 150 \text{ km s}^{-1}$) as seen in a spectrum toward Region 6 (Figure 3a) and a position-velocity diagram along the CH₃OH filament (Figure 3b). By assuming that both types of CH₃OH have the same beam-averaged column density ($N_{\text{CH}_3\text{OH}}$), the CH₃OH flux can be expressed by using the least squares method with the following equation (e.g., Martín et al. 2006a; Watanabe et al. 2014),

$$W_\nu = \sum_i \frac{8\pi^3 S_i \mu_0^2 \nu_i N_{\text{CH}_3\text{OH}}}{3kQ_{\text{rot}}} \left\{ 1 - \frac{\exp(h\nu_i/kT_{\text{rot}}) - 1}{\exp(h\nu_i/kT_{\text{bg}}) - 1} \right\} \times \exp\left(-\frac{E_{u,i}}{kT_{\text{rot}}}\right), \quad (1)$$

where W_ν is the flux density, S_i is the line strength, μ_0 is the dipole moment, ν_i is the frequency of the transition, Q_{rot} is the rotational partition function, k is the Boltzmann constant, h is the Planck constant, T_{bg} is the cosmic microwave background temperature ($= 2.73 \text{ K}$), and E_u is the upper state energy. We take the transition parameters necessary for calculating the equation (Table 1) from Splatalogue³ and the Cologne Database for Molecular Spectroscopy (CDMS⁴; Müller et al. 2001, 2005).

We performed the calculation for eleven apertures of 3" diameter along the filament shown in Figure 2, and an example for Region 6 is shown in Figure 4a. Parameters used for the calculation and the results are listed in Table 2. Each point in Figure 4a corresponds to the upper state column density of each unresolved transition, which decomposed by using the best-fit T_{rot} . The average T_{rot} is $7.4 \pm 0.5 \text{ K}$ for regions detected in both blended CH₃OH sets (i.e., Region 5–8). For regions without CH₃OH (2_K – 1_K) detection (Region 1–4 and 9–11), we used $T_{\text{rot}} = 7.4 \text{ K}$ to derive $N_{\text{CH}_3\text{OH}}$. The average $N_{\text{CH}_3\text{OH}}$ is $(2.3 \pm 1.0) \times 10^{14} \text{ cm}^{-2}$, although this is an average of the beam-averaged column densities due to uncorrected beam filling factor (η_{bf}). To ignore unknown η_{bf} effect, we divided the $N_{\text{CH}_3\text{OH}}$ by the H₂ column density ($N_{\text{CH}_3\text{OH}}/N_{\text{H}_2} = X_{\text{CH}_3\text{OH}}$) assuming that the N_{H_2} tracer has a same η_{bf} . In this paper, we employed the 880 μm dust continuum map (Figure 2a) to derive molecular gas mass (i.e., N_{H_2}) using the formulation described in Scoville et al. (2016). Assuming a constant dust temperature (T_{dust}) of 25 K, we derived $X_{\text{CH}_3\text{OH}}$ along the filament. As shown in Figure 4b, the $X_{\text{CH}_3\text{OH}}$ distribution is clearly peaked around Overlap (Region 6–8), whereas the AGN (Region 1) and SB (Region 3) positions show almost an order of magnitude lower values.

The errors shown in Figure 4b do not include the systematic uncertainty due to the 880 μm to N_{H_2} conversion.

The adopted T_{rot} of 7.4 K for Region 1–2 and 9–11 is consistent with the non-detections of the observed CH₃OH (2_K – 1_K) flux, although Region 3 and 4 should be detected when assuming 7.4 K. This might be attributed to (a) higher T_{rot} than 7.4 K and/or (b) CH₃OH (3_K – 2_K) overestimation due to a contamination from *c*-C₃H₂ (3_{12} – 2_{21}) emission. In case (a), since we need to increase T_{rot} to $\sim 10 \text{ K}$ at least, the derived $N_{\text{CH}_3\text{OH}}$ will decrease ($\sim 20\%$), and thus $X_{\text{CH}_3\text{OH}}$ will decrease. In case (b), the intrinsic CH₃OH (3_K – 2_K) fluxes will decrease 15% and 30% at Region 3 and 4, respectively, so that $X_{\text{CH}_3\text{OH}}$ will decrease. For both cases, $X_{\text{CH}_3\text{OH}}$ will decrease by a few tens of % around the eastern nucleus, so that our discussion and conclusion do not change. We note that the global $X_{\text{CH}_3\text{OH}}$ trend is robust even if AGN and SB have higher T_{rot} and T_{dust} conditions, since $X_{\text{CH}_3\text{OH}}$ only increases ~ 2 times at most when adopting $T_{\text{rot}} = 7.4$ – 14.8 K and $T_{\text{dust}} = 25$ – 50 K .

Comparing with CH₃OH observations toward giant molecular complexes in the spiral arm of M 51 with 1 kpc resolution ($X_{\text{CH}_3\text{OH}} \sim 3 \times 10^{-9}$; Watanabe et al. 2014) as a reference of the extragalactic (i.e., kpc-scale) quiescent regions, Region 1–3 of VV 114 show a few times lower $X_{\text{CH}_3\text{OH}}$, although Region 5–9 show a few times higher $X_{\text{CH}_3\text{OH}}$.

5. DISCUSSION & SUMMARY

To understand the characteristic CH₃OH distribution along the filament of VV 114, we compare $X_{\text{CH}_3\text{OH}}$ with star formation rate surface density (Σ_{SFR}) as shown in Figure 4c. We employed 110 GHz continuum (Saito et al. 2015) assuming that free-free (bremsstrahlung) emission dominates, and applied the free-free flux to SFR conversion (e.g., Yun & Carilli 2002). Such assumption is appropriate for starburst galaxies (e.g., M82; Condon 1992) and starburst-dominated LIRGs (e.g., NGC 1614; Saito et al. 2016). The 110 GHz image has a similar MRS ($\sim 21''$) and synthesized beam ($\sim 2''$) to CH₃OH images. We note that Σ_{SFR} for Region 1 and Region 2 are upper limits because of the presence of the putative AGN (i.e., contribution from nonthermal synchrotron emission). The derived log Σ_{SFR} shows a decreasing trend as a function of $X_{\text{CH}_3\text{OH}}$ with the correlation coefficient of -0.94 . When we exclude a putative AGN contribution (i.e., Region 2), the correlation coefficient becomes -0.97 . This can be explained by efficient photodissociation of CH₃OH due to massive star formation and putative AGN in the nuclear region (e.g., Martín et al. 2009) or desorption of CO (i.e., the precursor molecule of CH₃OH) from dust grain surfaces into gas-phase before forming CH₃OH molecules due to initial high temperature conditions. This is consistent with two orders of magnitude lower Σ_{SFR} at the spiral arm of M51 (Watanabe et al. 2014).

However, the photodissociation scenario is not enough to fully explain the CH₃OH distribution in VV 114, because Overlap shows higher $X_{\text{CH}_3\text{OH}}$ and also higher Σ_{SFR} than M51. Thus, we need another efficient mechanism, such as hot-core or shock, in order to explain high $X_{\text{CH}_3\text{OH}}$ at Overlap. Here we estimate a possible CH₃OH (2_K – 1_K) flux assuming that hot-

⁴ <http://www.astro.uni-koeln.de/cdms/catalog#partition>

core-like environments dominate Overlap. We used a single-dish measurement toward one of the local hot-cores NGC 2264 CMM3 (deconvolved major FWHM ~ 0.076 pc, $M = 40 M_{\odot}$, $I_{\text{CH}_3\text{OH}(2_K-1_K)} = 39.7 \text{ K km s}^{-1}$, $D = 738$ pc), which is believed to form a massive star of $8 M_{\odot}$ (Watanabe et al. 2015, and references therein). To account for all the molecular gas mass of Region 6 ($\sim 8.1 \times 10^8 M_{\odot}$) of VV 114, we need $\sim 2.0 \times 10^7$ CMM3. Since the $\text{CH}_3\text{OH}(2_K-1_K)$ flux of CMM3 at 87 Mpc is $\sim 2.9 \times 10^{-9} \text{ K km s}^{-1}$, the total flux of CMM3-like hot-cores at Region 6 is $\sim 0.058 \text{ K km s}^{-1}$. This is 0.5% of the observed $\text{CH}_3\text{OH}(2_K-1_K)$ flux at Region 6 ($11.9 \pm 1.4 \text{ K km s}^{-1}$). On average between Region 5 and Region 9, the possible contribution from hot-core-like environments is only 0.6%. When we use other representative hot-core environments OMC-1, Sgr B2(N), and Sgr B2(M) (Lis et al. 1993; Jones et al. 2008; Bally et al. 2011; Watanabe et al. 2015) instead of NGC 2264 CMM3, the contribution from hot-cores at Region 6 is still small (0.7-0.9%, 6.2%, and 23.5%, respectively). We list parameters used for these comparisons in Table 3. We note that the derived percentages are upper limits, because we assumed an extreme case that all gas masses contained in Region 6 are associated to hot-cores. Similar estimation of a possible CH_3OH flux from large collections of a molecular outflow from a massive star shows a similar conclusion (Meier et al. 2014). Therefore, we suggest that kpc-scale shocks are only applicable mechanisms to explain the high $X_{\text{CH}_3\text{OH}}$ at Overlap. Possible origin of the large-scale shocks is a gas-rich galaxy-galaxy collision, because Overlap is located between the progenitor's galaxies without apparent progenitor's spiral arms, bars, or nuclei. This shocked CH_3OH scenario at Overlap is consistent with the explanation of large velocity dispersion components of ionized gas detected at the same region (Rich et al. 2011). The shocked ionized gas shows the same systemic velocity as the CH_3OH . This shows the evidence that ionized gas shocks co-locate with molecular gas shocks at Overlap, indicating that merger-induced shocks can affect both molecular and ionized gas ISM.

In summary, merger-induced shocks are the most likely scenario to explain the kpc-scale CH_3OH filament (and large dispersion components of ionized gas) across the progenitors of VV 114. The $X_{\text{CH}_3\text{OH}}$ distribution peaks at Overlap, although the eastern nucleus, which har-

bors dense clumps associated with a compact starburst and a putative AGN, shows almost an order of magnitude lower abundances. $X_{\text{CH}_3\text{OH}}$ clearly anticorrelates with Σ_{SFR} , indicating that strong photodissociation (i.e., efficient destruction) or desorption of CO (i.e., inefficient production) on dust grains due to star-forming activities or AGN plays an important role to suppress CH_3OH emission at the nuclear regions. This is the first result of merger-induced shocks in molecular gas ISM through CH_3OH lines. As a future development, higher- J CH_3OH observations are required to address more realistic, finite optical depth and non-LTE excitation conditions (e.g., Goldsmith & Langer 1999; Mangum & Shirley 2015). Avoiding the multiple K -ladder blending, isolated transitions (e.g., $J_K = 0_0-1_{-1}$ at 108.89396 GHz) are also important. Follow-up observations of shock tracers in other wavelengths (e.g., near-IR warm H_2 ; Sugai et al. 1999; Herrera et al. 2012) can be used to confirm the shock scenario at Overlap. We will discuss other molecular lines detected and not detected in the Band 3 and Band 4 spectral scan in forthcoming paper.

The authors thank an anonymous referee for constructive comments that improved the contents of this paper. The authors thank S. Aalto, R. Aladro, P. Sanhueza, Y. Shimajiri, and K. Sliwa for useful discussion. T.S. and other authors thank ALMA staff for their kind support, and H. Nagai for the instruction of ALMA data reduction. T.S. and M. Lee are financially supported by a Research Fellowship from the Japan Society for the Promotion of Science for Young Scientists. T.S. was supported by the ALMA Japan Research Grant of NAOJ Chile Observatory, NAOJ-ALMA-0089, NAOJ-ALMA-0105, and NAOJ-ALMA-0114. R. Kawabe was supported by JSPS KAKENHI Grant Number 15H02073. D. Iono was supported by JSPS KAKENHI Grant Number 15H02074. This paper makes use of the following ALMA data: ADS/JAO.ALMA#2011.0.00467.S and ADS/JAO.ALMA#2013.1.01057.S. ALMA is a partnership of ESO (representing its member states), NSF (USA) and NINS (Japan), together with NRC (Canada), NSC and ASIAA (Taiwan), and KASI (Republic of Korea), in cooperation with the Republic of Chile. The joint ALMA Observatory is operated by ESO, AUI/NRAO, and NAOJ.

REFERENCES

- Aladro, R., Martín, S., Martín-Pintado, J., et al. 2011, *A&A*, 535, A84
- Aladro, R., Martín, S., Riquelme, D., et al. 2015, *A&A*, 579, A101
- Armus, L., Mazzarella, J. M., Evans, A. S., et al. 2009, *PASP*, 121, 559
- Bally, J., Cunningham, N. J., Moeckel, N., et al. 2011, *ApJ*, 727, 113
- Condon, J. J. 1992, *ARA&A*, 30, 575
- Costagliola, F., Aalto, S., Rodríguez, M. I., et al. 2011, *A&A*, 528, A30
- Costagliola, F., Sakamoto, K., Müller, S., et al. 2015, *A&A*, 582, A91
- Davis, T. A., Heiderman, A., Evans, N. J., & Iono, D. 2013, *MNRAS*, 436, 570
- Frayer, D. T., Ivison, R. J., Smail, I., Yun, M. S., & Armus, L. 1999, *AJ*, 118, 139
- Galametz, M., Zhang, Z.-Y., Immer, K., et al. 2016, arXiv:1606.06225
- García-Burillo, S., Usero, A., Fuente, A., et al. 2010, *A&A*, 519, A2
- Garrod, R. T., Wadlicus Weaver, S. L., & Herbst, E. 2008, *ApJ*, 682, 283-302
- Goldsmith, P. F., & Langer, W. D. 1999, *ApJ*, 517, 209
- Goldader, J. D., Meurer, G., Heckman, T. M., et al. 2002, *ApJ*, 568, 651
- Grimes, J. P., Heckman, T., Hoopes, C., et al. 2006, *ApJ*, 648, 310
- Henkel, C., Jacq, T., Mauersberger, R., Menten, K. M., & Steppe, H. 1987, *A&A*, 188, L1
- Herrera, C. N., Boulanger, F., Nesvadba, N. P. H., & Falgarone, E. 2012, *A&A*, 538, L9
- Ionon, D., Ho, P. T. P., Yun, M. S., et al. 2004, *ApJ*, 616, L63
- Ionon, D., Saito, T., Yun, M. S., et al. 2013, *PASJ*, 65, 7
- Jones, P. A., Burton, M. G., Cunningham, M. R., et al. 2008, *MNRAS*, 386, 117
- Lee, H.-H., Bettens, R. P. A., & Herbst, E. 1996, *A&AS*, 119, 111
- Lis, D. C., Goldsmith, P. F., Carlstrom, J. E., & Scoville, N. Z. 1993, *ApJ*, 402, 238

TABLE 1
INFORMATION OF THE DETECTED CH₃OH LINES AND THEIR IMAGING PROPERTIES

Transition	Blended J_K	ν_{rest} (GHz)	ν_{obs} (GHz)	E_u (K)	$S\mu^2$	Beam Size ($''$)	Beam P.A. ($^\circ$)	δv (km s $^{-1}$)	Noise rms ^a (mJy beam $^{-1}$)
2_K-1_K	$2_{-1-1-1}, E$	96.73936	94.88251	12.5	1.21	1.47×1.12	-88.8	50	0.37
	$2_{0-1_0}, A^{++}$	96.74138	94.88449	7.0	1.62				
	$2_{0-1_0}, E$	96.74455	94.88760	20.1	1.62				
	$2_{1-1_1}, E$	96.75551	94.89835	28.0	1.24				
3_K-2_K	$3_{0-2_0}, E$	145.09371	142.30873	27.1	2.42	1.60×1.04	$+67.8$	20	0.69
	$3_{-1-2-1}, E$	145.09737	142.31232	19.5	2.16				
	$3_{0-2_0}, A^{++}$	145.10315	142.31799	13.9	2.43				
	$3_{2-2_2}, A^{--}$	145.12441	142.33884	51.6	1.36				
	$3_{2-2_2}, E$	145.12619	142.34058	36.2	1.33				
	$3_{-2-2-2}, E$	145.12639	142.34078	39.8	1.35				
	$3_{1-2_1}, E$	145.13186	142.34614	35.0	2.21				
	$3_{2-2_2}, A^{++}$	145.13346	142.34772	51.6	1.36				

^a Noise rms in the data which have velocity resolution of δv .

TABLE 2
INFORMATION OF THE ROTATION DIAGRAM AND GAS AND STAR FORMATION PROPERTIES

ID	R.A. ($^\circ$)	Decl. ($^\circ$)	$S_{2_K-1_K} dv$ (Jy km s $^{-1}$)	$S_{3_K-2_K} dv$ (Jy km s $^{-1}$)	T_{rot}^a (K)	$N_{\text{CH}_3\text{OH}}$ (10^{14} cm $^{-2}$)	Σ_{SFR}^b (M_\odot kpc $^{-2}$ yr $^{-1}$)	$N_{\text{H}_2}^c$ (10^{22} cm $^{-2}$)	$X_{\text{CH}_3\text{OH}}$ (10^{-9})
1	16.9485	-17.5067	< 0.26	< 0.32	...	< 0.9	11.9 ± 0.5	4.7 ± 0.4	< 1.9
2	16.9482	-17.5070	< 0.27	0.29 ± 0.08	...	0.8 ± 1.2	28.2 ± 0.9	9.8 ± 1.0	0.8 ± 1.2
3	16.9478	-17.5072	< 0.26	0.68 ± 0.10	...	1.9 ± 1.5	27.0 ± 0.9	9.8 ± 1.0	1.9 ± 1.5
4	16.9474	-17.5072	< 0.27	0.85 ± 0.11	...	2.4 ± 1.6	14.1 ± 0.5	7.4 ± 0.6	3.2 ± 2.2
5	16.9470	-17.5072	0.44 ± 0.09	0.81 ± 0.11	6.1 ± 0.7	2.9 ± 1.7	9.5 ± 0.4	5.6 ± 0.5	5.1 ± 3.1
6	16.9465	-17.5073	0.51 ± 0.09	1.20 ± 0.12	7.8 ± 0.9	3.2 ± 1.6	7.5 ± 0.4	4.5 ± 0.5	7.2 ± 3.6
7	16.9461	-17.5074	0.57 ± 0.09	1.20 ± 0.11	7.0 ± 0.7	3.6 ± 1.6	6.2 ± 0.3	4.7 ± 0.4	7.6 ± 3.5
8	16.9457	-17.5075	0.33 ± 0.07	0.86 ± 0.11	8.9 ± 1.5	2.1 ± 1.2	4.9 ± 0.3	2.8 ± 0.3	7.6 ± 4.6
9	16.9453	-17.5076	< 0.26	0.56 ± 0.09	...	1.6 ± 1.3	5.5 ± 0.3	1.6 ± 0.3	9.5 ± 8.3
10	16.9449	-17.5076	< 0.26	< 0.32	...	< 0.9	6.5 ± 0.3	1.7 ± 0.3	< 5.4
11	16.9444	-17.5077	< 0.26	< 0.32	...	< 0.9	5.7 ± 0.3	1.4 ± 0.3	< 6.5

^a For regions without CH₃OH (2_K-1_K) detection, we adopt 7.4 K to derive $N_{\text{CH}_3\text{OH}}$.

^b Star formation rate surface density derived from the 110 GHz continuum emission (Saito et al. 2015).

^c Molecular hydrogen column density derived from the 880 μm dust continuum emission (Saito et al. 2015).

Lundgren, A., 2013, ALMA Cycle 2 Technical Handbook Version 1.1, ALMA
Mangum, J. G., & Shirley, Y. L. 2015, PASP, 127, 266
Martín, S., Mauersberger, R., Martín-Pintado, J., Henkel, C., & García-Burillo, S. 2006, ApJS, 164, 450
Martín, S., Martín-Pintado, J., & Mauersberger, R. 2006, A&A, 450, L13
Martín, S., Martín-Pintado, J., & Viti, S. 2009, ApJ, 706, 1323
Martín, S., Krips, M., Martín-Pintado, J., et al. 2011, A&A, 527, A36
Mathys, G., 2013, ALMA Cycle 2 Proposer's Guide, Version 1.8, ALMA
McMullin, J. P., Waters, B., Schiebel, D., Young, W., & Golap, K. 2007, Astronomical Data Analysis Software and Systems XVI, 376, 127
Meier, D. S., & Turner, J. L. 2005, ApJ, 618, 259
Meier, D. S., & Turner, J. L. 2012, ApJ, 755, 104
Meier, D. S., Turner, J. L., & Beck, S. C. 2014, ApJ, 795, 107
Müller, H. S. P., Thorwirth, S., Roth, D. A., & Winnewisser, G. 2001, A&A, 370, L49
Müller, H. S. P., Schlöder, F., Stutzki, J., & Winnewisser, G. 2005, Journal of Molecular Structure, 742, 215
Nakajima, T., Takano, S., Kohno, K., et al. 2015, PASJ, 67, 8
Nishimura, Y., Shimonishi, T., Watanabe, Y., et al. 2016, arXiv:1608.01099
Rabli, D., & Flower, D. R. 2010, MNRAS, 406, 95
Rich, J. A., Kewley, L. J., & Dopita, M. A. 2011, ApJ, 734, 87

Saito, T., Iono, D., Yun, M. S., et al. 2015, ApJ, 803, 60
Saito, T., Iono, D., Xu, C. K., et al. 2016, PASJ, 68, 20
Saitoh, T. R., Daisaka, H., Kokubo, E., et al. 2009, PASJ, 61, 481
Schutte, W. A., Tielens, A. G. G., & Sandford, S. A. 1991, ApJ, 382, 523
Scoville, N. Z., Evans, A. S., Thompson, R., et al. 2000, AJ, 119, 991
Scoville, N., Sheth, K., Aussel, H., et al. 2016, ApJ, 824, 63
Sliwa, K., Wilson, C. D., Krips, M., et al. 2013, ApJ, 777, 126
Sugai, H., Davies, R. I., Malkan, M. A., et al. 1999, ApJ, 527, 778
Takano, S., Nakajima, T., Kohno, K., et al. 2014, PASJ, 66, 75
Tateuchi, K., Konishi, M., Motohara, K., et al. 2015, ApJS, 217, 1
Teyssier, R., Chapon, D., & Bournaud, F. 2010, ApJ, 720, L149
Usero, A., García-Burillo, S., Martín-Pintado, J., Fuente, A., & Neri, R. 2006, A&A, 448, 457
Viti, S., Jimenez-Serra, I., Yates, J. A., et al. 2011, ApJ, 740, L3
Watanabe, N., Shiraki, T., & Kouchi, A. 2003, ApJ, 588, L121
Watanabe, Y., Sakai, N., Sorai, K., & Yamamoto, S. 2014, ApJ, 788, 4
Watanabe, Y., Sakai, N., López-Sepulcre, A., et al. 2015, ApJ, 809, 162
Wilson, C. D., Petitpas, G. R., Iono, D., et al. 2008, ApJS, 178, 189-224
Yun, M. S., Scoville, N. Z., & Knop, R. A. 1994, ApJ, 430, L109
Yun, M. S., & Carilli, C. L. 2002, ApJ, 568, 88

TABLE 3
CONTRIBUTION OF SOME REPRESENTATIVE HOT-CORES TO REGION 6

	Unit	NGC 2264 CMM3	OMC-1	Sgr B2(N)	Sgr B2(M)
Distance	pc	738	437	8.34×10^3	8.34×10^3
Mass	M_{\odot}	40	60-80	9100	2900
$I_{\text{CH}_3\text{OH}(2_K-1_K)}$	K km s^{-1}	39.7	309	907	1114
# of hot-core at Region 6		2.0×10^7	$(1.0-1.4) \times 10^7$	8.9×10^4	2.8×10^5
$I_{\text{CH}_3\text{OH}(2_K-1_K)}$ at 87 Mpc	K km s^{-1}	2.9×10^{-9}	7.8×10^{-9}	8.3×10^{-6}	1.0×10^{-5}
$I_{\text{CH}_3\text{OH}(2_K-1_K)}$ from hot-cores at Region 6	%	0.5	0.7-0.9	6.2	23.5

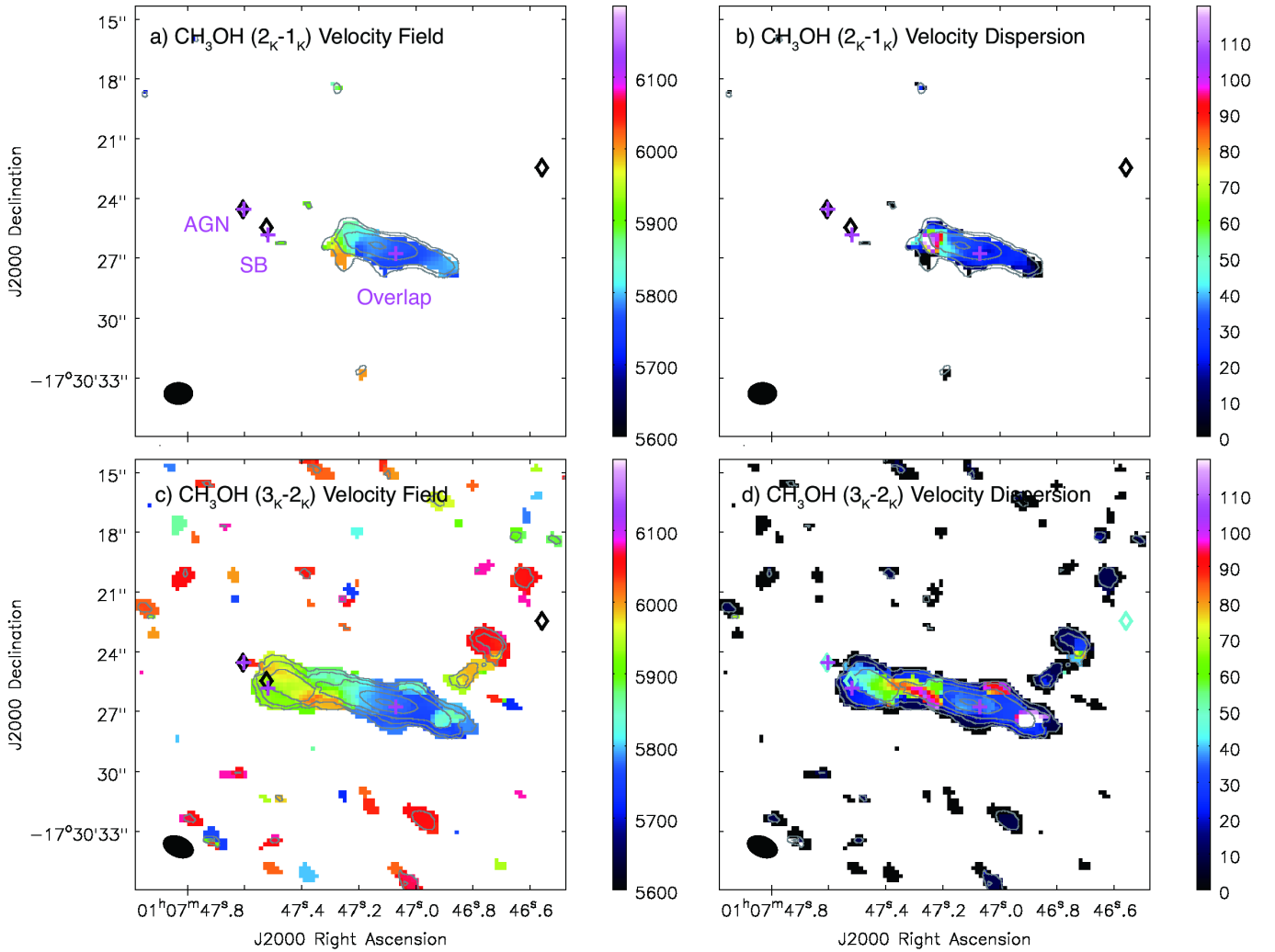


FIG. 1.— (a) Integrated intensity contour of CH_3OH (2_K-1_K) overlaid on the velocity field. The contours are $0.32 \times (0.16, 0.32, 0.64, \text{ and } 0.96)$ $\text{Jy beam}^{-1} \text{ km s}^{-1}$. (b) Same as (a) but for CH_3OH (3_K-2_K). The contours are $0.67 \times (0.08, 0.16, 0.32, 0.64, \text{ and } 0.96)$ $\text{Jy beam}^{-1} \text{ km s}^{-1}$. The crosses show the peak positions of the HCO^+ ($4-3$) emission. AGN, SB, and Overlap correspond to E0, E1, and W0 defined by Iono et al. (2013), respectively. The synthesized beams are shown in the bottom-left corner. The diamonds show the K_s -band stellar nuclei.

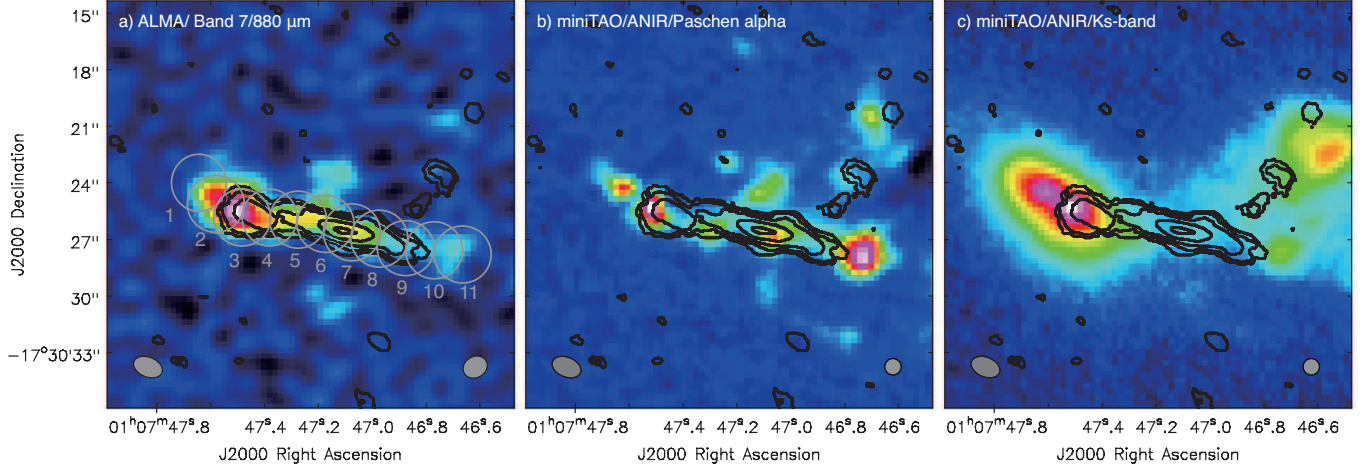


FIG. 2.— Integrated intensity contour of CH₃OH (3_K-2_K) overlaid on (a) 880 μ m dust emission, (b) Paschen α emission, and (c) K_s-band (Saito et al. 2015; Tateuchi et al. 2015). The synthesized beam of the CH₃OH (3_K-2_K) image is shown in the bottom-left corner. The beam size of each color image is shown in the bottom-right corner. The eleven gray circles shown in Figure 2a are used for the photometry along the filament.

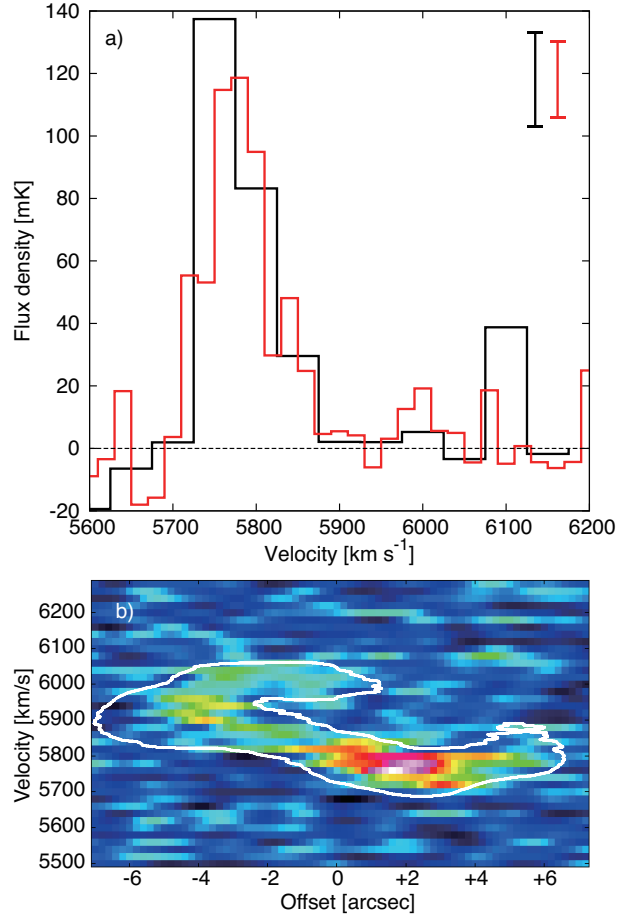


FIG. 3.— (a) Observed spectrum of CH₃OH (2_K-1_K) (black) and CH₃OH (3_K-2_K) (red) toward Region 6 (see Figure 2a). The bars shown in the top right represents a typical statistical error bars associated with the data. (b) Position-velocity diagram of CH₃OH along the filament of VV 114 (position angle = 79.4°, length = 14.2'', and width = 1''.8). The white outline shows the 20 σ contour of CO (1–0) (Saito et al. 2015).

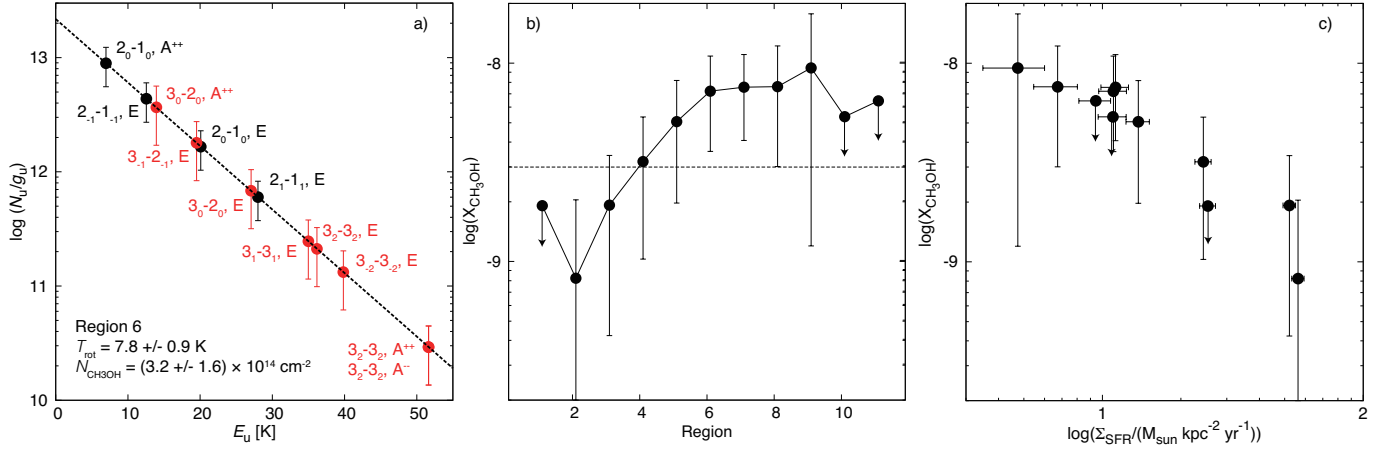


FIG. 4.— (a) Rotation diagram of CH_3OH for Region 6. Black and red points show $J = 2-1$ and $3-2$ transitions, respectively. The dotted line shows the best-fit. (b) $X_{\text{CH}_3\text{OH}}$ distribution along the dust filament of VV 114. The arrows show the 3σ upper limits. The dashed line shows $X_{\text{CH}_3\text{OH}} \sim 3 \times 10^{-9}$, which is the value for the spiral arm of M51 using $\sim 1 \text{ kpc}$ aperture (Watanabe et al. 2014). (c) $X_{\text{CH}_3\text{OH}}$ as a function of Σ_{SFR} .